NASA CONTRACTOR REPORT

NASA CR-1286

THEORETICAL COMPARISON OF BEADS, WIRES, AND FILMS AS ROCKETSONDE TEMPERATURE SENSORS IN THE MESOSPHERE

by Forrest L. Staffanson

Prepared by
UNIVERSITY OF UTAH
Salt Lake City, Utah
for Langley Research Center

NATIONAL AERONAUTICS AND SPACE ADMINISTRATION • WASHINGTON, D. C. • FEBRUARY 1969

NASA CR-1286

THEORETICAL COMPARISON OF BEADS, WIRES, AND FILMS AS ROCKETSONDE TEMPERATURE SENSORS IN THE MESOSPHERE

By Forrest L. Staffanson

Issued by Originator as Report No. UTEC MR-67-055

Prepared under Grant No. NGR-45-003-025 by
UNIVERSITY OF UTAH
Salt Lake City, Utah

for Langley Research Center

NATIONAL AERONAUTICS AND SPACE ADMINISTRATION

For sale by the Clearinghouse for Federal Scientific and Technical Information
Springfield, Virginia 22151 – CFSTI price $3.00

TABLE OF CONTENTS

LIST OF FIGURES

LIST OF TABLES

INTRODUCTION

Analysis of current rocketsonde sensors using film-mounted thermistor beads shows that the film mount rather than the thermistor bead is the dominating element in the performance of the sensor in the higher altitudes of operation. Since in this case the bead is essentially only measuring the film temperature, attention is drawn more toward the film rather than the bead as the sensing link with the air. The relationship of the film temperature to the environment becomes of greater importance than that of the bead temperature. In a similar way, bead thermistors with long wires depend strongly on the heat transfer properties of the wire at the higher altitudes.

Efforts to increase the altitude capability of rocketsonde atmospheric temperature sensors have lead to the consideration of different geometric shapes of the sensor element. Generally, the sensor shape has been restricted to those of commercially available thermistor devices which feature sufficient structural strength when made very thin, such as beads on wires, rods, wafers, etc. Thinness is needed to minimize heat conduction along the structure to supporting framework, and is required for response speed. The time lag of a sensor is proportional to its volume-to-surface ratio and, therefore, to its thickness. The thinnest of commercially available thin thermistor devices has been the miniature bead (on wires). Beads of about 10 mil diameter are in common use. Thinness in other sensor shapes and structures, particularly in the flat plate and circular cylinder, becomes feasible with the availability of thin substrates and the prospect of reliable thermistor films applicable to these substrates. It is anticipated that a small area of thermistor film located, for example, on a thin cylindrical filament or on a thin planar sheet, at a point sufficiently distant from supporting structure, will enable the detection of the filament or sheet temperature without the use of a thermistor bead. Other films on the substrate would provide electrical conduction to the thermistor film and desirable thermal radiation properties for the sensor.

Shape influences, in addition to sensor mass, the air flow over its surface. Characteristics of the hydrodynamic process of air encountering the sensor surface determine first the magnitude of the temperature rise in the air during its deceleration at the surface, and second the thermal sensitivity of the surface to the temperature of the decelerated air. Furthermore, the heat input to the sensor from each segment of the radiation environment depends on the sensor cross section presented to that segment, so, as one might expect, the integrated input depends on the shape of the surface. Finally, the temperature rise due to electric heating of the thermistor depends on the rate at which heat can be conducted away from the thermistor area. Since conductive heat dissipation from a source point in a thin solid body depends on the dimensionality and boundaries of the body, it is expected that the electric heating error will depend on sensor shape.

The purpose of the present discussion is to compare parameters, which depend on shape and which influence performance, for three basic sensor shapes: the small sphere, the thin circular cylinder in cross-flow, and the thin flat plate in parallel flow. The significance of relative weakness or merit is indicated in terms of sensor temperature error where appropriate. The analysis and results are intended for application in future sensor improvements as well as in better understanding of the performance of current devices. The discussion addresses itself, for example, to the question: Since at the higher altitudes the current film-mounted sensors are dominated by the temperature of the film, how does the film temperature relate to the air temperature, and how does it compare with the bead temperature in representing the air temperature, at all altitudes of operation?

For quantitative comparisons arbitrary sensor specifications and environmental conditions are chosen. The thickness dimension

$D = 3.2 \times 10^{-4}$m (12.6 mil, the nominal 10 mil bead)

$d = 2.5 \times 10^{-5}$m (1 mil wire or filament)

$\delta = 1.27 \times 10^{-5}$m (0.5 mil Mylar film)

is chosen to be as thin as practical for the respective shape. The volume specific heat

$(\rho c)_b = 3.31 \times 10^6$ joule/m^3 (thermistor materials [Wagner, 1961])

$(\rho c)_w = 2.71 \times 10^6$ joule/m^3 (Pt-Ir wire (2.44×10^6 for quartz) [CRC Handbook, 1960])

$(\rho c)_f = 1.84 \times 10^6$ joule/m^3 (Mylar [Dupont Bulletin M-2B])

corresponds to a material commonly used for the respective shape. For uniformity in absorptivity and emissivity each of the three shapes is assumed to have a thin opaque coat of aluminum with solar absorptivity, long-wave absorptivity, and emissivity:

$$\alpha_s = 0.15$$

$$\alpha = \epsilon = 0.08 \text{ [CRC Handbook 1966]}$$

The air flow and radiation environment is approximately that encountered by a sensor mounted on a stable parachute-sonde system having weight and dimension of the ARCAS system and falling in the altitude interval 90 to 50 km. Air properties are based on the U. S. Standard Atmosphere 1962 and air speed is based on the empirical parachute drag coefficient developed by Eddy [1965]. Air speeds are listed versus altitude in Table II.

AERODYNAMIC HEATING

Sensor temperature is governed by the heat equation

$$(\rho c) \; \frac{v}{A} \; \dot{T} = h\left(T(\mathrm{env}) + r\,\frac{V^2}{2c_p} - T\right) + \frac{q_r}{A} - \epsilon\sigma T^4$$

Electric heating and thermal conduction terms are omitted until later in the discussion. The solution T(t) of this equation is the temperature of the sensor in regions remote from boundaries and internal heat sources.

The sensor is sensitive to the atmospheric temperature T(env) only through its contact with the aerodynamically heated air at its surface. The corresponding air temperature is called the recovery temperature:

$$T_r = T(env) + r \frac{V^2}{2c_p}$$

Aerodynamic heating or viscous dissipation arises from the conversion of kinetic energy to thermal energy in the deceleration of the air at the sensor surface. The recovery factor, r, depends on the shape of the surface. Theoretical values of r for the three shapes are found in the literature and are verified by experiment for the regimes of continuum flow and free molecule flow [Schaaf and Chambre, 1961]. Available data indicate that linear interpolation on the basis of Knudsen number is adequate between these regimes, i.e., through the regimes of slip and transition flow. Figure 1 shows the relative effect of aerodynamic heating for the three shapes. Values used for the recovery factor are listed in Table II.

The recovery factor in free molecule flow is larger than in continuum flow, so the interpolated value increases as mean free path (and altitude) increases. Knudsen number is the dimensionless ratio of mean free path to a characteristic dimension of the body or of the flow field. The greater surface dimension of the flat plate assures for it a smaller Knudsen number and, therefore, smaller recovery factor. The flat plate, in other words, is nearer continuum flow than is the thin cylinder or sphere. It is estimated that the variability and

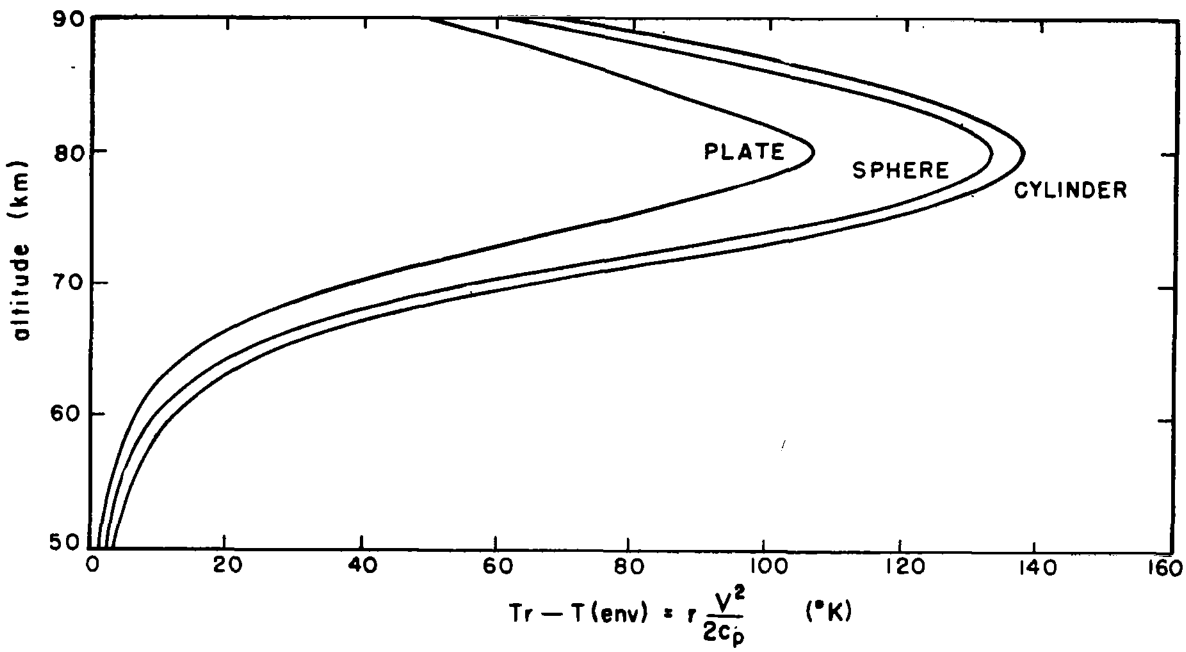

Fig. 1. Relative effect of aerodynamic heating for three shapes.

uncertainty in recovery factor are about the same for the three shapes and, therefore, the error in correcting flight data for aerodynamic heating is expected to be proportional to the magnitude of the correction. Laboratory tests with real planar sensors are recommended, since the possible occurrence of flutter, wrinkling of the film, or other deviations from ideal geometry might diminish the apparent advantage shown here. It would appear that the plate at least is not inferior to the other shapes with respect to aerodynamic heating.

With a given recovery factor and air speed, a thermometer at best can assume the associated recovery temperature. Aside from aerodynamic heating, the sources of thermometric error are dynamic lag, radiant heating or cooling, and electric heating due to instrument monitoring current and radio frequency currents induced by the sonde transmitter. Error sources associated with the transducing or detecting function of the thermistor, i.e., the errors in reading out the sensor temperature, are not reflected in the heat equations nor included in this discussion. Effects of photoconductivity in the sensor, and anomalous changes in the thermistor resistivity due to physical or chemical effects or thermal history, for example, are excluded.

TIME CONSTANT

Linearizing the quartic term in the heat equation leads to the form

$$\tau \dot{T} + T = T_e$$

where the time constant is

$$\tau = \frac{(\rho c)(v/A)}{h + 4\epsilon\sigma T_a^3}$$

and the equilibrium sensor temperature (the sensor temperature excluding dynamic errors) is

$$T_e = \frac{h\ T_r + (q_r/A) + 3\ \epsilon\sigma T_a^4}{h + 4\ \epsilon\sigma T_a^3}\ ,\quad T_a \approx T_e$$

The time constant depends on sensor shape through the thickness parameter (v/a) and through the convection coefficient h.

The convection coefficient h, like recovery factor, varies inversely with the hydrodynamic characteristic dimension of the surface. Values as seen in Table II decrease in the order: cylinder, sphere, plate. The relative difference, however, decreases considerably at higher altitudes where h becomes smallest and most critical. The convection coefficient for the plate approaches those of the cylinder and sphere in spite of the effect of increased decay length in the plate.

The maximum local value of h in a plate is found at the leading edge, where, therefore, the thermistor is assumed to be located. However, the temperature gradient in the plate, associated with the varying local h, is reduced by the conductivity of the plate. Thus, conduction tends to average the leading edge temperature with that of the neighboring area of the plate downstream. The distance downstream over which the leading edge temperature is averaged depends on the magnitude of convection with the air stream relative to conduction in the plate, i.e., on the decay length

$$\lambda_f^{-1} = \sqrt{k\delta/2\left(h + 4\ \epsilon\sigma T_a^3\right)}$$

The effective h at the leading edge is, therefore, an average of the local h over a plate length downstream proportional to the decay length. The values of h given in Table II for the plate include this effect.

The characteristic length L_f used in calculating h for the plate (film) was taken as $3\lambda_f^{-1} \pm 0.1$ cm, while, of course, those for the sphere and cylinder were their respective constant diameters. Values of L_f associated with the h_f are included in Table II. At a given altitude, h for a given aerodynamic shape increases with decreasing L until L becomes small relative to the molecular mean free path, where h is independent of L. Therefore, increasing decay length in the plate tends to decrease h. Even so, as mentioned, at higher altitudes, the deterioration of the plate convection coefficient is not as rapid as those of the sphere and cylinder.

The overriding factor regarding comparative time constant is (v/A), which assumes the values D/6, d/4, $\delta/2$ respectively for the sphere, cylinder, and plate, or, in ratio, 53.:6:6 in our numerical example. Though the denominators would favor the sphere, the numerators (thickness parameter) give the plate and cylinder by far the advantage. The values of (ρc) are not expected to change this conclusion significantly. Comparison of time constants is illustrated in Fig. 2 and Table II.

RADIATION ERROR

At equilibrium ($\dot{T} = 0$) the linearized heat equation above reduces to two terms representing the competition between the convective and radiative heat transfer processes

$$h\left(T_r - T_e\right) + 4\,\epsilon\sigma T_a^3\left(T_R - T_e\right) = 0 \qquad T_a \approx T_e$$

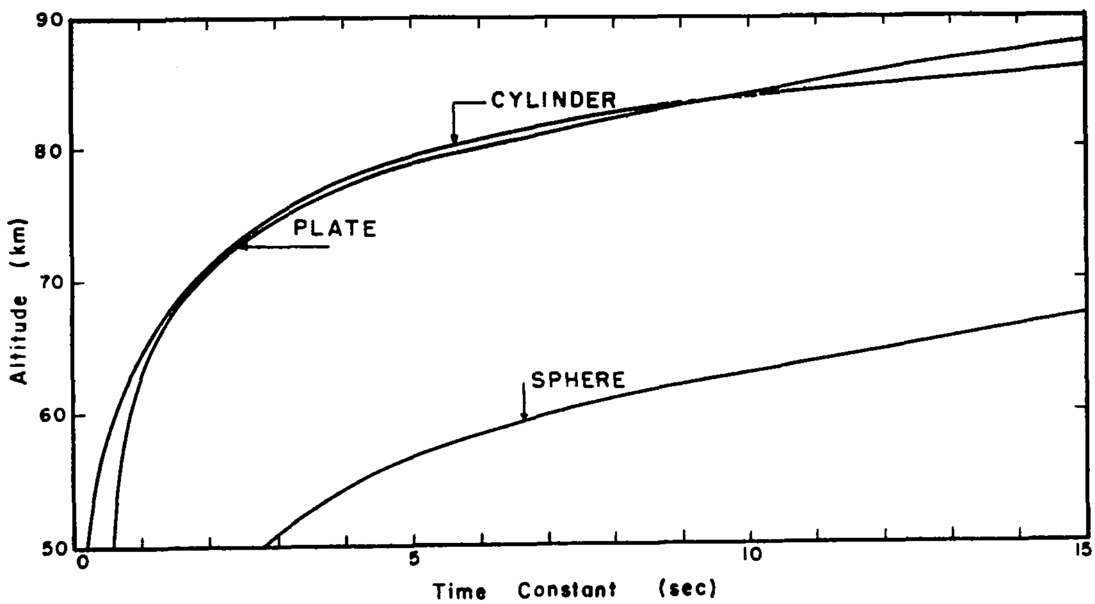

Fig. 2. Comparison of time constant for three sensor shapes.

T_r and T_R are the temperatures the sensor tends toward, by linear extrapolation, due to the presence of the air stream and radiation environment, respectively. The radiation temperature is given by

$$T_R = \frac{\left(q_r/A\right) + 3\ \epsilon\sigma T_a^4}{4\ \epsilon\sigma T_a^3}$$

The sensor temperature T_e lies at a point between T_r and T_R according to the ratio of the coefficients

$$u = \frac{h}{4\ \epsilon\sigma T_a^3}$$

as shown in Fig. 3. The quantity u acts as a weighting factor between

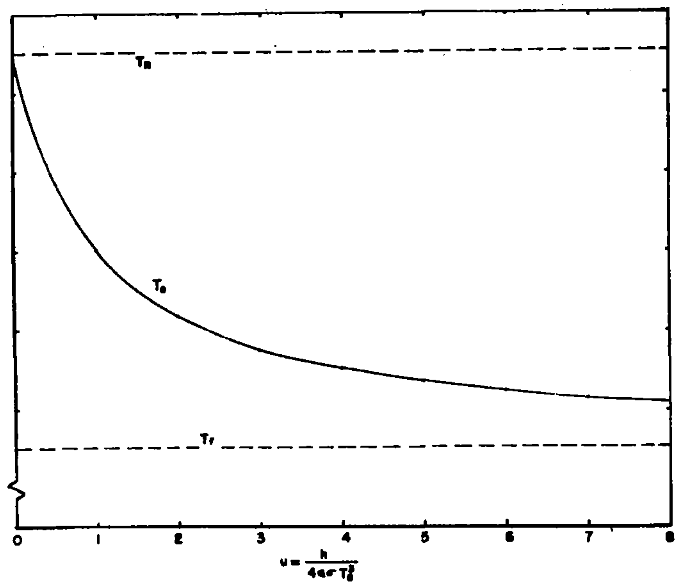

Fig. 3. The dependence of T_e on the ratio of the convection and radiation coefficients.

the two environmental temperatures,

$$T_e = \frac{uT_r + T_R}{u + 1}$$

and gives the radiation error per unit difference between T_R and T_r:

$$\frac{T_e - T_r}{T_R - T_r} = \frac{1}{u + 1}$$

Values of u and $(u + 1)^{-1}$ are included in Table II. The dependence of u on shape is primarily that of h which has been discussed.

Turning now to the dependence of the radiation temperature T_R on shape, we first give the general expression for the radiative heat input term of the heat equation:

$$\frac{q_r}{A} = \frac{1}{A} \int_A \int_\Omega \cos\theta \; dS \; \frac{d\Omega}{\pi} \int_o^\infty \alpha_\lambda \, \epsilon_\lambda \, E_{b\lambda}(t) \; d\lambda$$

where

α_λ = spectral absorptivity of the sensor

ϵ_λ = spectral emissivity of the source in $d\Omega$

$E_{b\lambda}(T)$ = Planck radiant energy spectral distribution function for the source in $d\Omega$ at temperature T

Ω = solid angle subtended by the environment

A = total sensor surface area

θ = angle between sensor surface element dA and the direction toward $d\Omega$

λ = radiation wavelength

Consider the four principal environmental radiation sources seen by the sensor:

j = 1 sun

j = 2 earth and atmosphere as a reflector of solar radiation

$j = 3$ earth and atmosphere as a long wave source

$j = 4$ sonde parts in view of the sensor; or shield

Assuming the radiant emittance

$$I_j = \int_0^\infty \epsilon_{\lambda j} \, E_{b\lambda}(T_j) \, d\lambda$$

and the mean absorptivity

$$\bar{\alpha}_j = \frac{\int_0^\infty \alpha_{\lambda j} \epsilon_{\lambda j} E_{b\lambda}(T_j) \, d\lambda}{I_j}$$

are independent of angle, the geometric factor f_j

$$f_j = \frac{1}{A} \int_A \int_{\Omega_j} \cos\theta \, dA \, \frac{d\Omega_j}{\pi}$$

may be calculated separately and treated as a multiplicative factor, so the radiation input term takes the form

$$\frac{q_r}{A} = \sum_j{}' \, \bar{\alpha}_j \, f_j \, I_j$$

The influence of shape on T_R enters only through the geometric factor f_j.

The relative value of f_1 is simply the ratio of the illuminated cross section, A_r, to the total sensor surface area, A

$$\frac{A_r}{A} = \frac{1}{4}\ ,\ \frac{\sin\psi}{\pi}\ ,\ \frac{\cos\psi}{2}$$

for the sphere, cylinder and plate, respectively, where ψ is the angle between the sensor axis and the solar line of sight.

No attempt is made to compare f_2 between shapes. Inhomogeneity and variability in the indirect solar radiation are estimated to render meaningless such a comparison. The magnitude of the uncertainty, however, can be reduced with the use of a cylindrical shield. Radiation entering the forward opening of the shield would least affect a plate sensor with leading edge toward the opening. The shielding advantage of a plate is discussed below.

The geometric factors associated with the earth long-wave radiation are comparable, if no shield is present, due to symmetry. The earth occupies essentially the lower hemisphere of the sensor's total view and for any of these sensor shapes the corresponding geometric factor is approximately 1/2. Again, however, as will be shown, a cylindrical shield would reduce this geometric factor most for the plate.

Finally, f_4 illustrates the advantage of a plate oriented edge-on ($\gamma = \pi/2$) toward a radiation source. Figure 4 shows $f_4(\theta_o)$ for the three shapes when the sonde surfaces occupy a "polar cap" with half-angle θ_o as shown in the figure. A half-angle of 35° was chosen for computation purposes in this discussion.

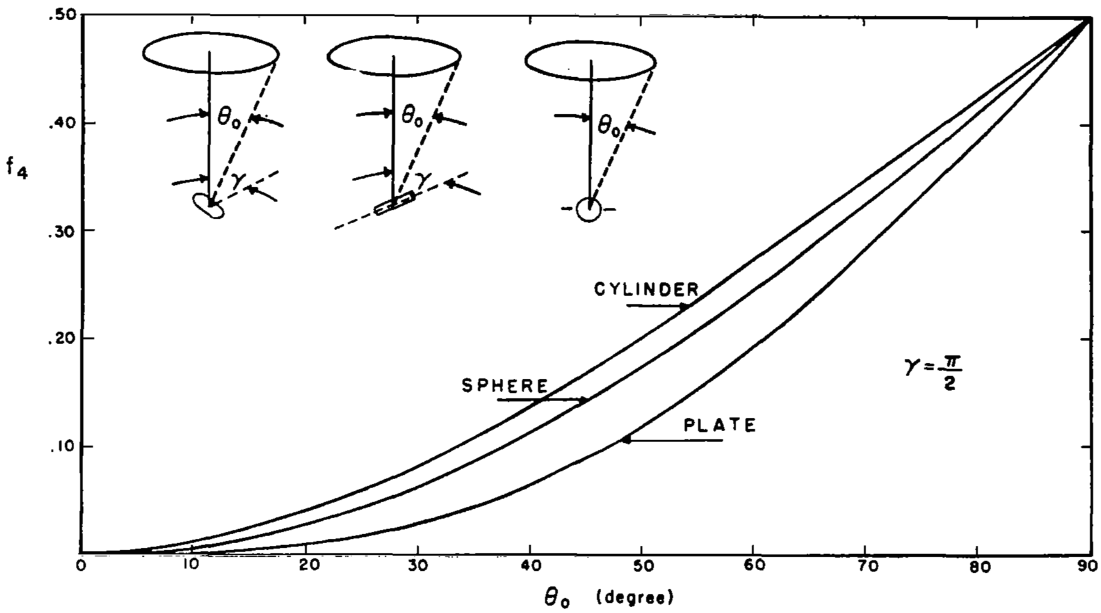

Fig. 4. Geometric factor for the three sensor shapes of a circular region located 90 degrees from the sensor axis subtending half-angle θ_o.

Comparison of the f_j relative to shape (values are not comparable within a column) is shown in Table I for the unshielded sensor. The influence of shape enters only through f_1 and f_4. Exceptions to this occur to the extent that the earth does not occupy a hemispherical solid angle at the sensor and is not a uniform source. If the sensor returns frequently to equilibrium in sun-shaded portions of its descent, and since the radiant heating from the sonde is negligible (see below), then, aside from the above exceptions, sensor shape has little effect on T_R.

Comparative values of T_R are shown in Table II and Fig. 5, along

TABLE I

APPROXIMATE RELATIVE MAGNITUDES OF THE

GEOMETRIC FACTORS

Source	F_j(Sphere)	:	F_j(Cylinder)	:	F_j(Plate)
Sun	1/4	:	0-1/π	:	0-1/2
Albedo	1	:	1	:	1
Earth	1	:	1	:	1
Sonde	9	:	11	:	4

TABLE II

NUMERICAL RESULTS

Z(Km)		50	60	70	80	90
T(env)		271	256	220	181	181
V(m/sec)		60.9	121	291	444	300
L_f(cm)		0.22	0.22	0.35	0.66	0.87
h $\frac{\text{watt}}{{}^\circ\text{K}-\text{m}^2}$	b	63.8	24.4	7.72	2.17	.28
	w	91.8	26.9	8.89	2.51	.31
	f	24.9	14.6	5.98	1.60	.25
r	b	1.17	1.35	1.39	1.34	1.43
	w	1.66	1.68	1.54	1.39	1.51
	f	.86	.89	.92	.98	1.09
T_r - T(env) (°K)	b	2.16	9.84	58.9	133	64.2
	w	3.08	12.2	65.2	138	68.0
	f	1.60	6.44	39.0	97.2	48.8
τ (sec)	b	2.8	7.1	22.0	65	265
	w	.18	.62	1.8	5.5	29.3
	f	.46	.78	1.9	5.8	19
T_e (°K)	b	273	266	280	310	277
	w	274	269	286	315	277
	f	273	263	261	282	271
u	b	173	72	19.5	4.0	.77
	w	247	77	21.0	4.4	.80
	f	68	44	18.5	3.9	.69
$(u + 1)^{-1}$	b	.0057	.014	.044	.20	.58
	w	.0040	.013	.045	.18	.56
	f	.0145	.022	.051	.20	.59
T_R (°K)	b	301	304	299	298	300
	w	301	303	299	299	300
	f	300	304	305	298	300

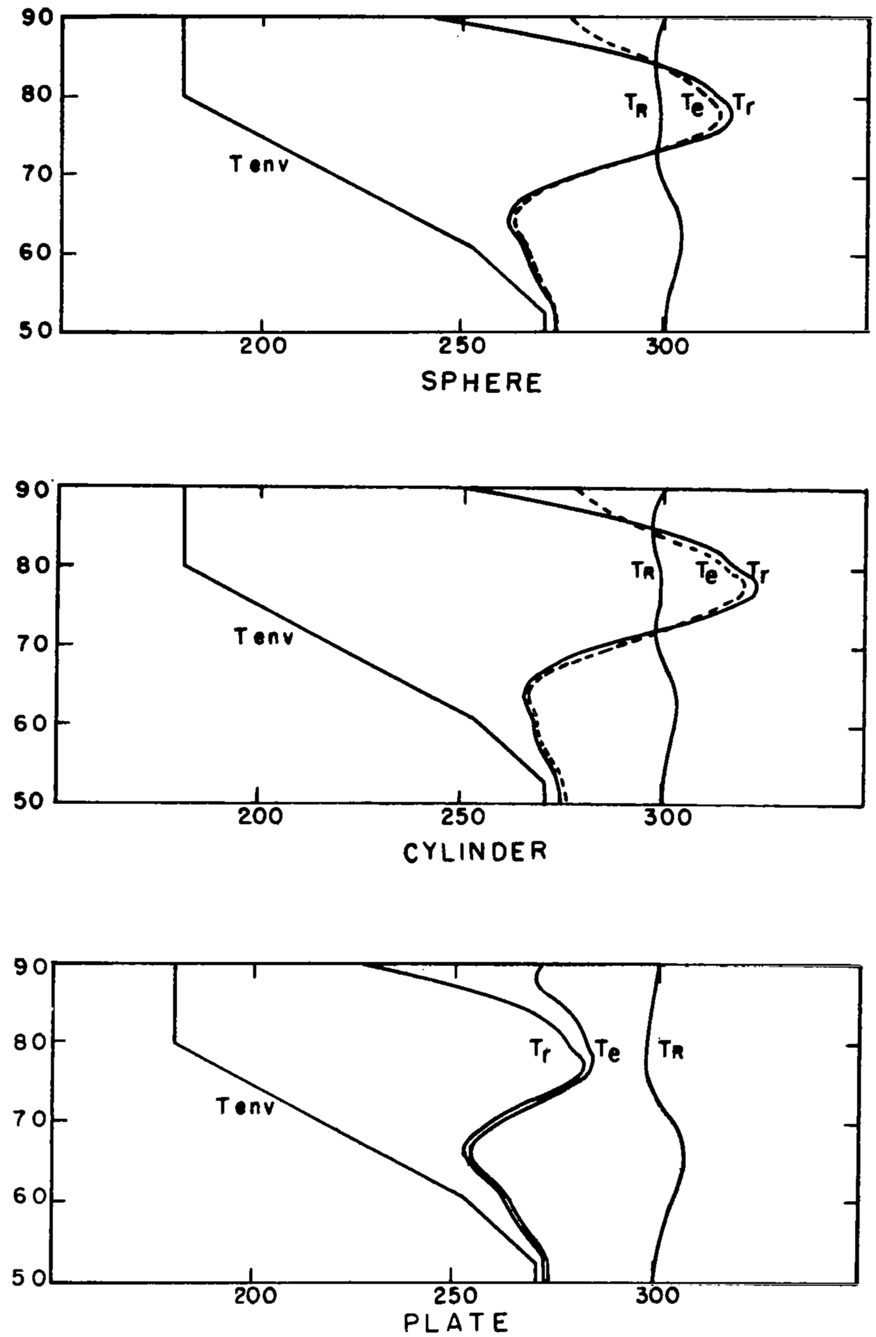

Fig. 5. Illustration of T_R, T_r, and T_e, and T(env) for the three sensor shapes.

with the corresponding values of recovery temperature, air temperature, and sensor equilibrium temperature. The computed T_R in Table II exclude direct solar illumination of the sensor. This is consistent with the usual practice of reading flight data at minima as it oscillates between sunlit and shaded values. The thermometric effect of each of the radiation sources on each shape sensor is indicated in Table III, where variations in T_R and T_e are listed corresponding to ± 100 percent variations in the heat input from each radiation source. Introducing a perturbation factor β_j, the heat input to the sensor from the jth source is $\beta_j \alpha_j f_j I_j$, and the day-shade case cited above is represented by $\beta_j = 0,1,1,1$ according to the order $j = 1,2,3,4$. The values in Table III are arranged in quadruplets

$$\begin{Bmatrix} \left(T_e^- - T_e\right) & \left(T_e^+ - T_e\right) \\ \left(T_R^- - T_R\right) & \left(T_R^+ - T_R\right) \end{Bmatrix}$$

where the temperatures are based on β-values as follows:

$$\beta_j = \left.\begin{cases} \left.\begin{matrix} 0 & i \neq 1 \\ 1 & i = 1 \end{matrix}\right\} & \text{for } T^- \\ 2 & \text{for } T^+ \end{cases}\right\} \text{ when } j = i$$

$$= \left.\begin{cases} 1 & j \neq 1 \\ 0 & j = 1 \end{cases}\right\} \text{ otherwise}$$

TABLE III

VARIATION IN SENSOR EQUILIBRIUM TEMPERATURE T_e AND RADIATION TEMPERATURE T_R FOR 100 PERCENT VARIATION IN THE HEATING FROM EACH RADIATION SOURCE

	Z(km)	50		60		70		80		90	
i = 1 (Sun)	b	.8	1.6	2.1	4.3	6.5	12.9	19.0	37.4	64.6	110.9
		141.2	279.9	149.2	291.7	122.8	230.0	84.8	147.2	78.4	124.4
	w	.8	1.5	2.5	5.0	7.2	14.4	21.3	41.9	76.2	128.5
		178.5	354.2	184.8	359.9	146.7	273.3	102.1	174.6	93.3	144.6
	f	3.5	7.0	7.8	15.2	16.0	38.7	49.8	93.9	119.1	185.1
		275.5	530.7	289.3	533.4	267.0	453.3	163.3	239.4	122.8	184.8
i = 2 (Albedo)	b	-.5	.4	-1.1	1.1	-3.4	3.4	-10.3	10.1	-47.9	36.8
		-75.1	74.3	-81.6	79.1	-71.5	66.5	-57.1	47.9	-91.9	48.1
	w	-.3	.3	-1.0	1.1	-3.0	3.0	-9.1	8.9	-45.2	35.5
		-74.3	73.8	-79.4	77.2	-67.0	63.1	-54.2	46.5	-90.4	48.4
	f	-.9	.9	-2.0	2.0	-4.2	4.2	-14.1	13.7	-53.8	40.5
		-75.5	74.1	-85.0	80.3	-87.3	79.5	-75.5	57.6	-97.0	47.6
i = 3 (Earth)	b	-.1	.1	-.3	.3	-1.0	.9	-2.9	2.9	-12.3	11.4
		-21.4	21.3	-23.1	22.5	-19.8	19.4	-15.2	14.4	-19.2	16.1
	w	0.0	.1	-.3	.3	-.9	.9	-2.7	2.6	-12.0	11.1
		-21.6	21.6	-23.1	22.5	-19.1	18.8	-14.9	14.3	-19.6	16.5
	f	-.2	.3	-.5	.6	-1.1	1.2	-3.8	3.8	-13.0	11.9
		-20.5	20.4	-22.9	21.7	-22.8	22.3	-18.4	17.1	-18.3	15.2
i = 4 (Sonde)	b	0.0	0.0	0.0	0.0	0.0	0.0	0.0	0.0	-.1	0.0
		-.1	0.0	-.1	.1	-.1	0.0	-.1	0.0	-.1	0.0
	w	0.0	0.0	0.0	0.0	0.0	0.0	0.0	0.0	-.1	0.0
		-.1	.1	-.1	.1	0.0	.1	0.0	.1	-.1	.1
	f	0.0	0.0	0.0	0.0	0.0	.1	0.0	0.0	0.0	0.0
		-.1	0.0	-.1	0.0	0.0	.1	-.1	0.0	0.0	0.0

Thus the temperature variations are referred to the dayshade value at each altitude. The differences for i = 1 correspond to bringing the sensor into the sunshine "broadside" to the rays for T^- and to doubling the solar absorption for T^+. For $i \neq 1$, T^- corresponds to eliminating the associated source and T^+ to doubling the absorption from that source.

The sensitivity to radiation is seen to be greatest in the plate. This apparent disadvantage is least at the higher altitudes, according to the behavior h. Radiant heating from the sonde seems to be negligible over the entire altitude interval for all sensors. This suggests that the radiant heat input from a shield would be small.

As mentioned above, unshielded sensors during a daytime flight may be exposed to direct sunlight intermittently and with varying aspect according to the motion of the parachute systems. If the sensor's time constant is small enough, its colder values will correspond to shade equilibrium ($\beta_1 = 0$). Larger τ, however, prevents the sensor from returning to the shade equilibrium values between exposures to the sun. For example, if we require the sensor to return to within 20 percent of its equilibrium value in one-half the period of a 5 cps parachute rotation, then τ must be less than $2.5/(\ell n\ 0.2) = 1.6$ sec. Immersion temperature sensors under this requirement are limited to about 70 km altitude. At 70 km, 20 percent of the temperature variation due to solar radiation is of the order of 5°K, depending on solar absorptivity and aspect angle. This limitation may be overcome with adequate dynamic corrections or with a shield. The strong emittance of the sun serves to amplify uncertainty associated with aspect angle, solar absorptivity, and the time function of solar exposure, so that for future higher altitudes the shield seems preferable, if not mandatory.

The curves of Fig. 4 apply to the open end of a circular cylindrical radiation shield as well as to f_4. Quantative comparison of the susceptibility to the entering radiation is given by the curves of Fig. 6, which are the ratios of f_4 between shapes. The advantage of the plate in such a shield is seen to increase considerably for deeper positions in the shield.

The directional sensitivity of a given sensor to radiation can be represented by an imaginary closed surface about the sensor (analogous to a radio antenna pattern) whose radial distance from the sensor in

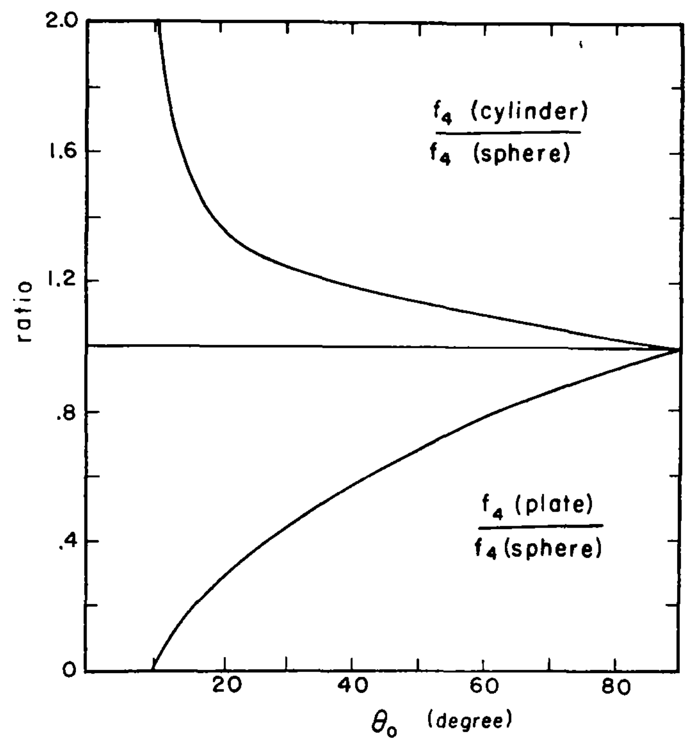

Fig. 6. Geometric factors of Fig. 4 for cylinder and plate relative to that of the sphere versus θ_o.

each direction is proportional to the sensitivity in that direction. The magnitude of the sensitivity in a given direction is the geometric factor of the sensor for a small element $d\Omega$ in that direction when surrounded by a uniform source. For such an incremental source the geometric factor reduces to

$$df = \frac{d\Omega}{\pi} \; \frac{A_r}{A}$$

where A_r is the sensor cross section in the specified direction. The three-dimensional sensitivity surfaces for the sphere, cylinder, and plate are therefore

$$\frac{1}{4}, \; \frac{\sin\theta}{\pi}, \; \frac{\cos\theta}{2}$$

where θ is the angle between the source direction and the sensor axis. This surface is spherical (omnidirectional) for the spherical sensor, toroidal for the cylinder, and is a double sphere for the plate. Figure 7 illustrates, with a sectional view of the sensitivity surfaces, the relative shielding effect of a given shield as it varies with sensor shape. It is seen that the plate benefits most from the shield, and that the cylinder benefits even less than the sphere. The disadvantage of the cylinder is due to its unfavorable orientation within the shield, which is assumed dictated by structural and hydrodynamic requirements.

A shield with a downward view half-angle of $\theta = 35°$ would reduce f_2 and f_3 to 0.087, 0.108, and 0.044 respectively for the sphere,

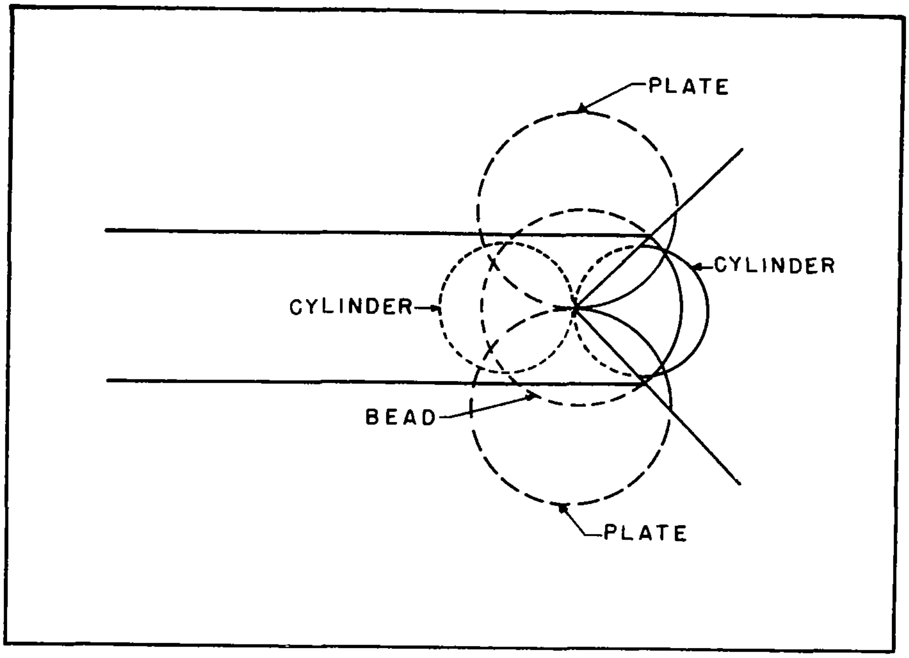

Fig. 7. Sectional view of the sensitivity surfaces of the three sensor shapes, illustrating the relative susceptibility to radiation entering a cylindrical shield.

cylinder, and plate. The reduction in radiant heating from each source would be 100 percent for direct solar radiation for all sensors, approximately 78 percent, 73 percent, and 89 percent respectively for albedo, and 79 percent, 75 percent, and 89 percent respectively for earth long-wave radiation. The increased heating from the sonde (shield) would remain negligible. Results of calculations using the shield are shown in Appendix Fig. A4. The geometric factor advantage of the plate is overcome by its convection coefficient disadvantage for altitudes below 87 km. Smaller shield view half-angle would lower this altitude if found feasible within the entry length and shield size requirements [ref. Progress Report UTEC MR 67-046, August 1967].

ELECTRIC HEATING ERROR

Since electric heating will occur in a small area on the sensor occupied by the thermistor, the associated temperature rise will depend on conductive dissipation into the neighboring regions of the sensor. The heat equation for the small thermistor region of the sensor is

$$(\rho c)(v/A)\dot{T} = h\left(T_r - T\right) + q_r/A - \epsilon\sigma T^4 + W/A + k\left(A_o/A\right) T_o'$$

where

W/A = ohmic power dissipated per sensor area

k = thermal conductivity of the sensor

A_o = cross-sectional area of conductive path at the edge of the thermistor region

T_o' = sensor temperature gradient at the edge of the thermistor region

In general, the conductive term is linear in T and in a conduction temperature T_k

$$k\left(A_o/A\right) T_o' = H_k\left(T_k - T\right)$$

so that the equilibrium temperature of the sensor with electric heating becomes

$$T_e = \frac{h\, T_r + 3\epsilon\sigma\, T_a^4 + H_k\, T_k}{h + 4\epsilon\sigma\, T_a^3 + H_k}$$

The following four cases are considered (Fig. 8): a thermistor bead on long wires (B - W), a thermistor bead connected by short wires to a large planar film (B-W-F), a short thermistor film on a thin cylindrical

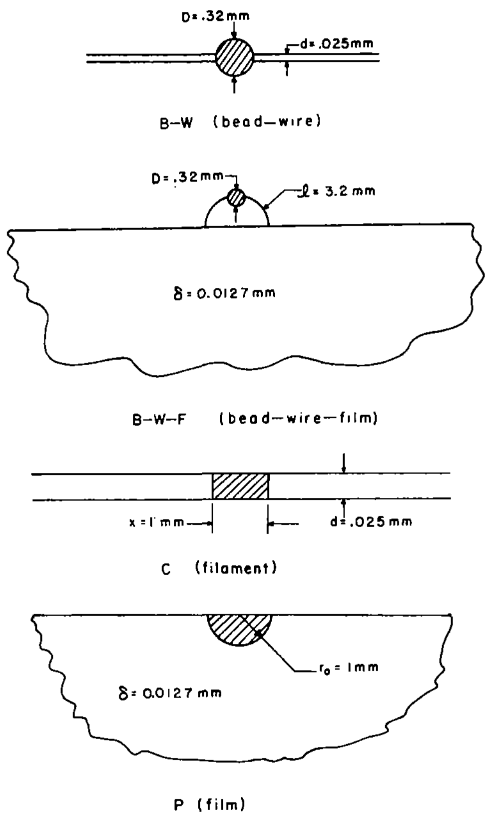

Fig. 8. Illustration of the four cases used to evaluate the effect of sensor shape on electric heating error.

filament (C), and a thermistor film on the leading edge of large plastic film (P). The expression for the conductive coefficient H_k and the conduction temperature T_k is given in Table IV, along with that for the surface area A in each case. Quantities in Table V are further

TABLE IV

CONDUCTIVE PARAMETERS FOR THE FOUR SELECTED SENSOR TYPES

	B-W	B-W-F	C	P
H_k	$C_{wb}\lambda_w$	$C_{wb}\lambda_w \dfrac{\lambda_f' \cosh \lambda_w \ell + C_{wf} \lambda_w \sinh \lambda_w \ell}{\lambda_f' \sinh \lambda_w \ell + C_{wf} \lambda_w \cosh \lambda_w \ell}$	$k_c \dfrac{d}{2x} \lambda_c$	$k_f \dfrac{\delta}{r_o} \lambda_f'$
T_k	T_{we}	$A_1 T_{fe} + B_1 T_{we}$	T_{we}	T_{fe}
A	πD^2	πD^2	$\pi\ x\ d$	$\pi\ r_o^2$

defined as follows:

$$\lambda_{f,p} = \sqrt{\frac{2\left(h_f + 4\ \sigma T_{af}^3\right)}{k_f \delta}}, \quad \lambda_w = \sqrt{\frac{4\left(h_w + 4\ \sigma T_{aw}^3\right)}{k_w d}}, \quad \lambda_c = \sqrt{\frac{4\left(h_w + 4\ \sigma T_{ac}^3\right)}{k_c d}}$$

$$\lambda_{f,p}' = \lambda_f \frac{K_1(\lambda_f\ r_o)}{K_o(\lambda_f\ r_o)}$$

$$C_{wb} = \frac{k_w}{2} \left(\frac{d}{D}\right)^2$$

$$C_{wf} = \frac{(kd)_w}{(k\delta)_f} \frac{d}{2r_o}$$

x, r_o = length, radius of thermistor region

$A_1 = \lambda_f'/\left(\lambda_f' \cosh \lambda_w \ell + C_{wf} \lambda_w \sinh \lambda_w \ell\right)$

$B_1 = 1 - A_1$

and $K_o(x)$ and $K_1(x)$ are modified Bessell functions of the second kind of order zero and one, respectively.

The electric heat W generated in the detector (thermistor region of the sensor) is dissipated through immediate convection and radiation and through conduction into the neighboring region of the sensor. The associated temperature rise of the detector is given by

$$\Delta T = \frac{\partial Te}{\partial W} W = \frac{W}{\left(h + 4\epsilon\sigma T_a^3 + H_k\right)A} = \frac{W}{S}$$

The denominator S is the "dissipation constant" (which is "constant" only when the environment is constant) for the thermistor and is tabulated in Table V along with the temperature error for a 10 μ watt electric power disspation W.

Values used for thermal conductivity of the filament and film assume bulk conductivity of fused quartz, Mylar, and aluminum [Powell et al., 1966]. The aluminum coating was assumed to be 100 mμ thick.

Notice the advantage afforded by the two-dimensional conductive

TABLE V

COMPARATIVE ELECTRIC HEATING ERROR $\Delta T(°K)$, $S(\mu\ watt/°K)$

Altitude (km)		50	60	70	80	90
BW*	ΔT	0.24	0.52	1.07	2.08	3.86
	S	41.6	19.4	9.30	4.80	2.59
BWF	ΔT	.24	0.47	.76	0.98	1.09
	S	42.1	21.4	13.1	10.2	9.15
C	ΔT	0.64	1.49	2.93	5.50	10.0
	S	15.7	6.72	3.41	1.82	1.00
F	ΔT	.04	.05	.07	.09	0.11
	S	273.	206.	151.	108.	95.2

path in the plate, and the disadvantage of the limited dissipation afforded by the filament. The dissipative quality of the film is seen also in comparing the bead-wire and bead-wire-film cases, even under the handicap of a smaller conductivity. No effort was made here to optimize the metallic film for least electric heating error against time constant and conduction from supports. The influence of shape is nevertheless apparent.

CONCLUSION

From the theoretical comparison of the thermometric performance of the three basic sensor shapes, it is found that the two-dimensional or planar shape (with both sides ventilated) appears generally the most promising for future immersion sensor designs. Its principal

*Note that if the wire ends cut off at the bead were left long, the bead-wire error might be halved.

features are: small recovery factor associated with its larger aerodynamic characteristic length, small thermal mass associated with its thinness, greater potential for shielding associated with its favorable pattern of radiation sensitivity, and larger "dissipation constant" (lower electric heating error) associated with its two-dimensional conduction.

The cylindrical sensor features comparable time constant but has larger recovery factor and, therefore, more aerodynamic heating, smaller shielding payoff, and a greater sensitivity to electric heating.

In general, the properties of the sphere lie between those of the plate and cylinder, except for the excessive time constant. The time constant of the sphere disqualifies it from consideration as a sensor for the higher altitudes, though it may serve as the detector of the film temperature in lieu of the potentially much better film thermistor. This interim use of the bead is practical due primarily to the strong dissipative quality of the film which enables it to "force" the bead.

At the lowest altitudes of the mesosphere, above which relatively few sondes currently reach, differences due to shape are unimportant because sufficient convective coupling and low enough air speed tend to diminish the temperature difference between the sensor and air. The larger solar heating suffered by the film (even at the lower altitudes) is offset by its faster response which allows discrimination of this error from the signal.

APPENDIX A

COMPARATIVE PERFORMANCE UNDER SELECTED PERTURBATIONS

The quantitative effects of reduced air speed on recovery temperature T_r, and of the 35° circular cylindrical shield on radiation temperature T_R for each of the shapes are illustrated in Figs. A1, A2, and A3. The corresponding sensor equilibrium temperature T_e and air temperature T(env) are shown also. These computed curves differ from those of Fig. 5 due only to changes in the air speed V and the geometric factors f_2, f_3, and f_4, according to Table A1.

TABLE A1

PERTURBATION INPUTS

		Fig. 5	Fig. A1	Fig. A2	Fig. A3
V		V	V/2	V	V/2
f_2	b	.400	.400	.087	.087
	w	.400	.400	.108	.108
	f	.400	.400	.044	.044
f_3	b	.420	.420	.087	.087
	w	.430	.430	.108	.108
	f	.400	.400	.044	.044
f_4	b	.087	.087	.913	.913
	w	.108	.108	.892	.892
	f	.044	.044	.956	.956

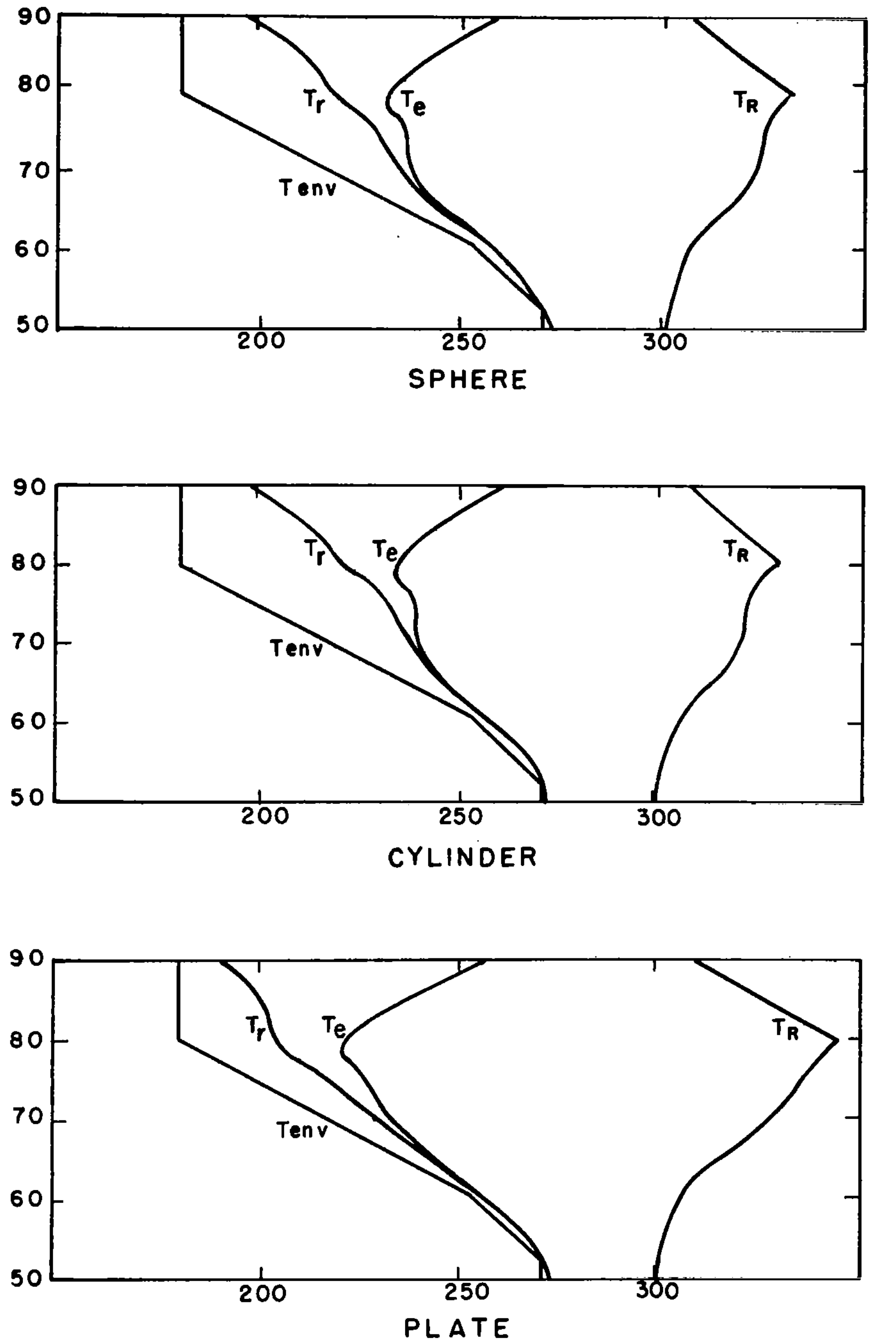

Fig. A1. Temperature functions under 50 percent reduction in air speed.

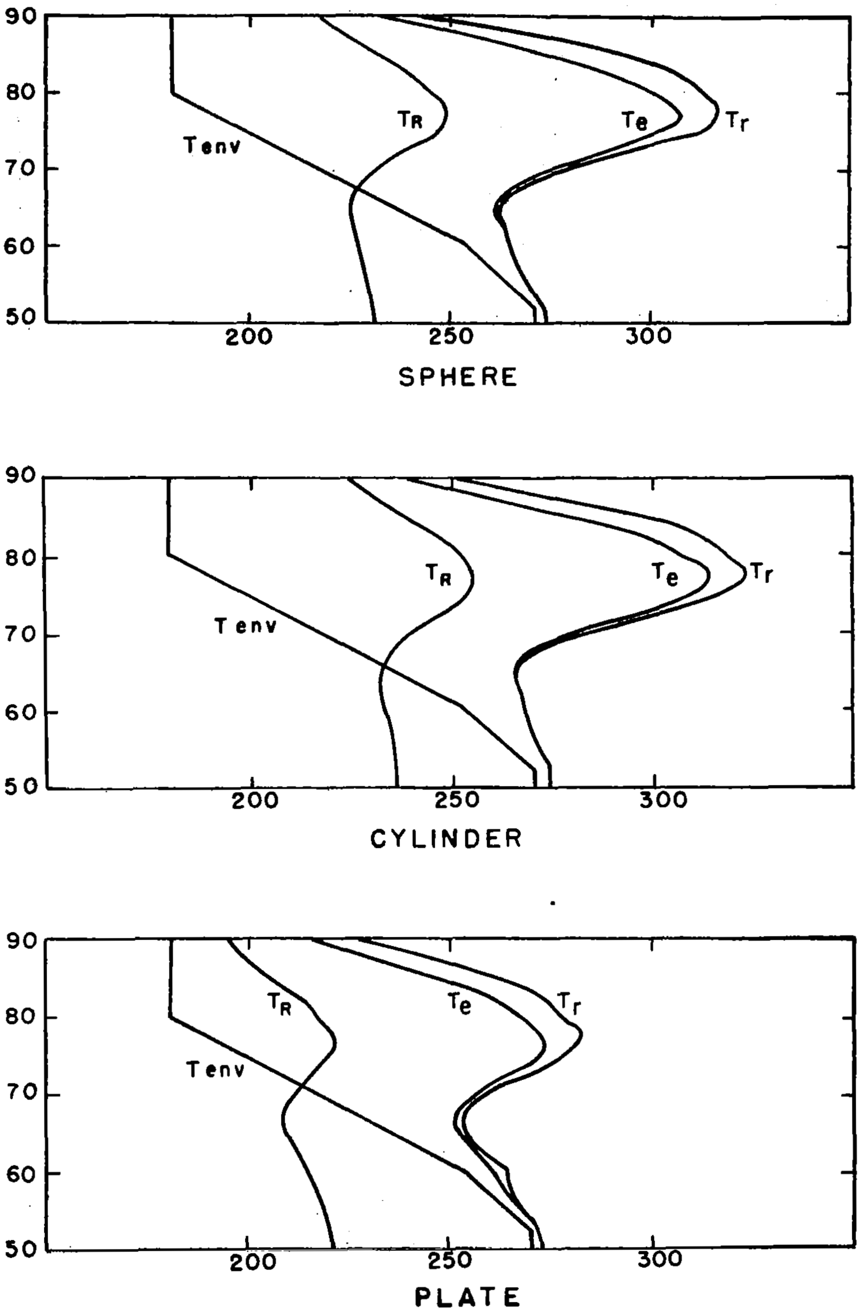

Fig. A2. Temperature functions for the shielded plate.

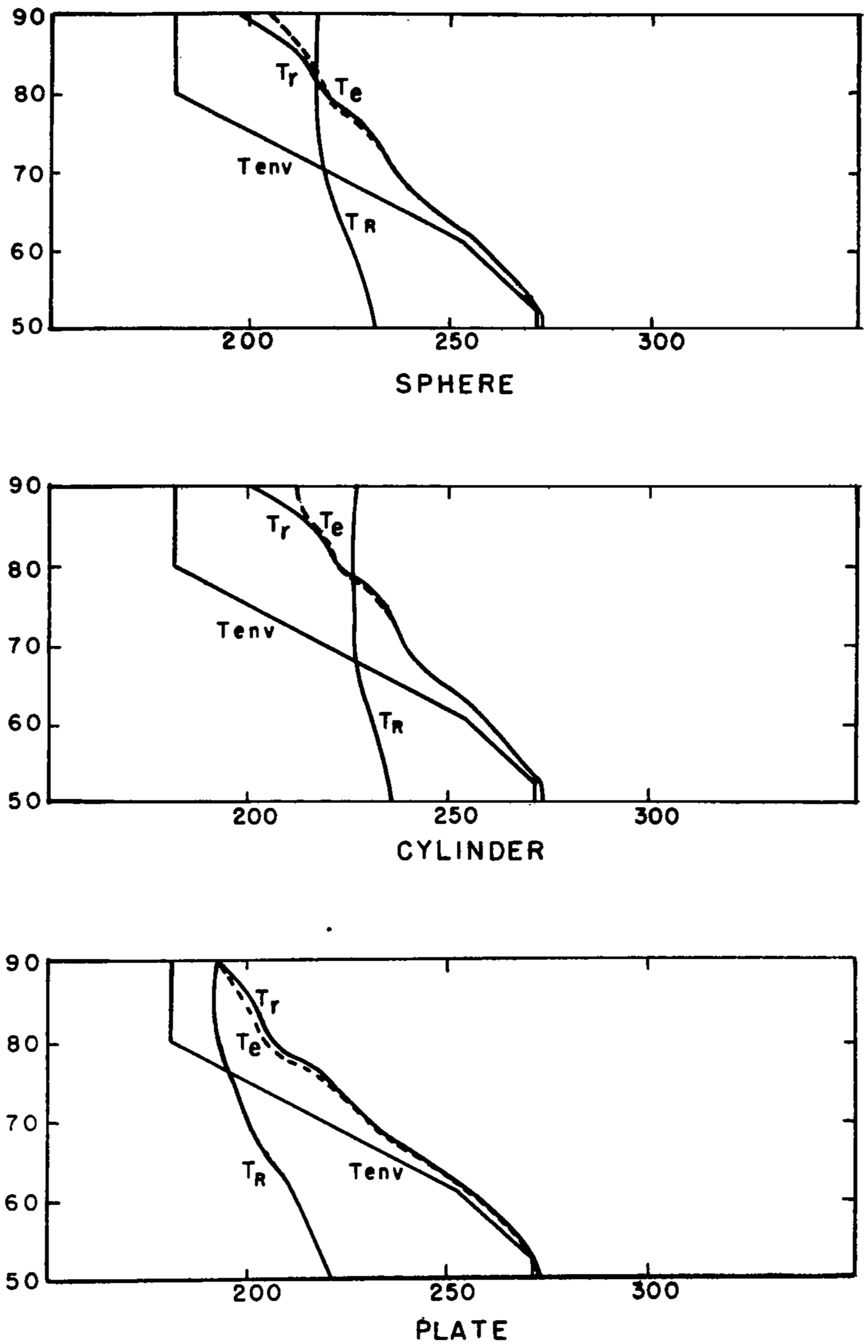

Fig. A3. Temperature functions with 50 percent speed reduction and a shield.

The comparative reduction in radiation error variability (uncertainty) associated with a shield is illustrated in Fig. A4. The curves show the variation in T_e corresponding to a ± 20 percent variation in albedo and earth infrared heat input to the sensor, for the unshielded sensor (but shaded from direct sunshine) and for the shielded sensor. Notice that the shield is unnecessary at the lower altitudes.

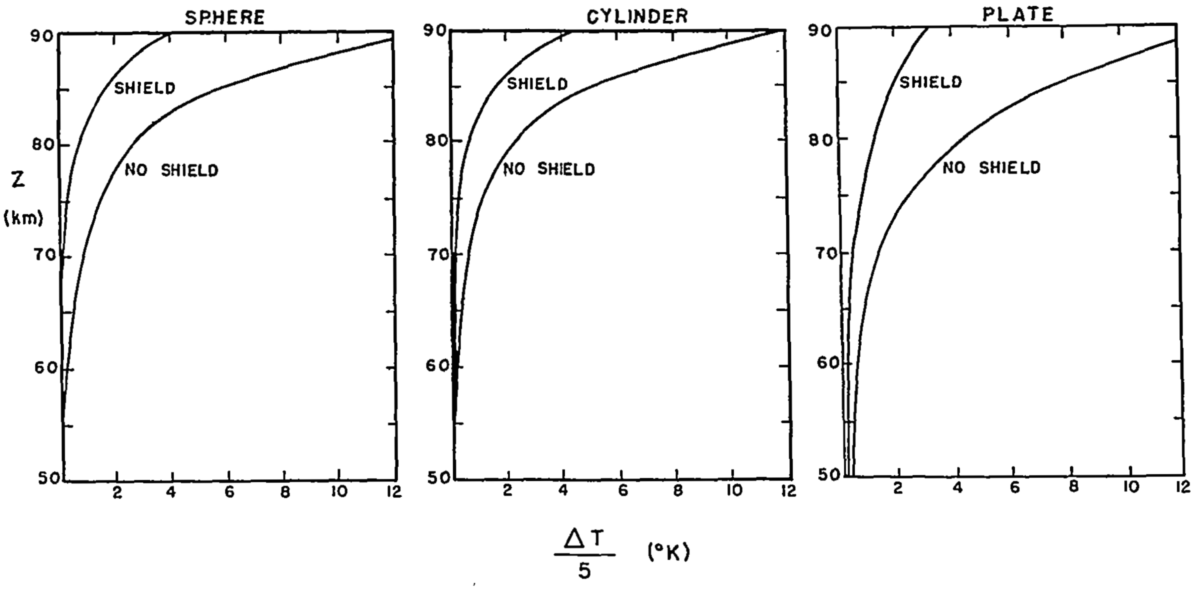

Fig. A4. Curves of one-fifth the difference between equilibrium temperatures with and without albedo and earth long wave radiation for both the shielded and unshielded sphere, cylinder, and plate.

$$\Delta T = 0.2 \left[T_e \left(\beta_j = 0111 \right) - T_e \left(\beta_j = 0001 \right) \right]$$

APPENDIX B

LOCAL CONVECTION COEFFICIENTS IN THE PLATE

The convection coefficient h, as has been mentioned, varies from point to point along the flow over the sensor surface. The temperature at a point would depend on the local value of h, except that thermal conduction in the sensor body tends to average the temperature in the vicinity. Small diameter in the case of the bead and wire allows the use of a single mean value of h, for given flow conditions, the average over the entire circumference along the flow. However, in the case of the film in parallel flow, the airstream passes over an extended surface, regions of which may be more or less conductively isolated. Thus the leading edge may assume a temperature quite different from that of the trailing edge.

The convection coefficient h for the plate is the mean value of the local coefficient h_x:

$$h = \frac{1}{L} \int_0^L h_x \, dx$$

Given the function h for a sequence of lengths x_i along the plate, the corresponding function h_x may be obtained by differencing:

$$\left(h_x\right)_i = \frac{x_i \; h_i - x_{i-1} \; h_{i-1}}{x_i - x_{i-1}}$$

Figure B1 shows the local convection coefficient obtained in this way from the convection coefficient derived from the literature and discussed in another progress report in preparation. The curves indicate the increased values at the leading edge for selected altitudes and air speeds. Figure B2 illustrates the dependence of h_x on air speed.

When the conductivity-thickness product $k\delta$ of a film is sufficiently small, the temperature distribution along the flow approaches the shape of $h_x T_R$. Figure B3 shows the difference in plate temperature under selected conditions (Z = 80 km, V = 225 m/sec, and Z = 70 km, V = 260 m/sec for an aluminum-coated 0.5 mil Mylar film in a nighttime descent.) Plate equilibrium temperature T_e is found on the center line of the film sufficiently inside of the sideposts. About 5°K temperature difference is seen between the leading and trailing edge of the 3 cm film. The example shows the leading edge to be nearer the recovery temperature than is the trailing edge at both altitudes.

Figure B3 also illustrates a case in which the recovery temperature T_r increases from a value less than T_R (80 km) to one greater than T_R (70 km). The radiation environment in this case at 70 km causes a cooling effect which, though it tends to bring the sensor toward T(env) from T_r, is nevertheless an error. Notice also that the increased decay length at 80 km tends to decrease the size of the central region of the film which is isolated from the support posts.

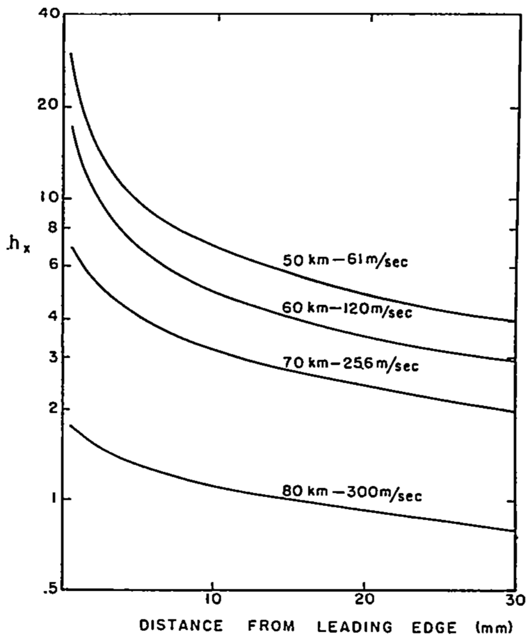

Fig. B1. Variation of local convection coefficient from the leading edge of a flat plate.

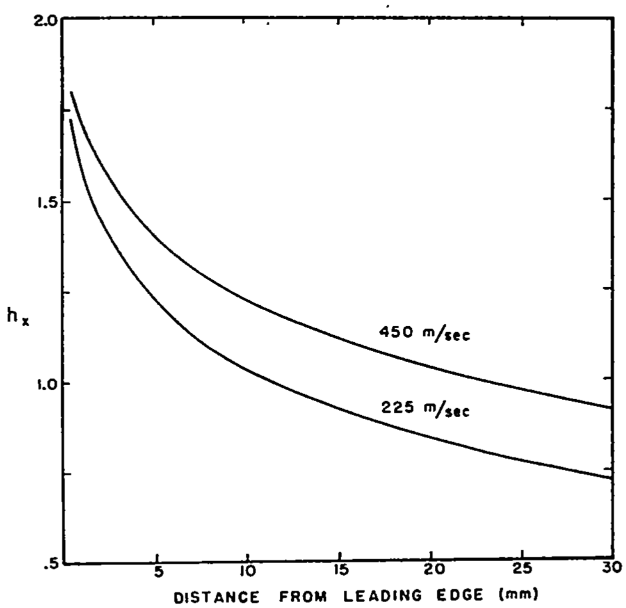

Fig. B2. Deviation of local convection coefficient with air speed at 80 km altitude.

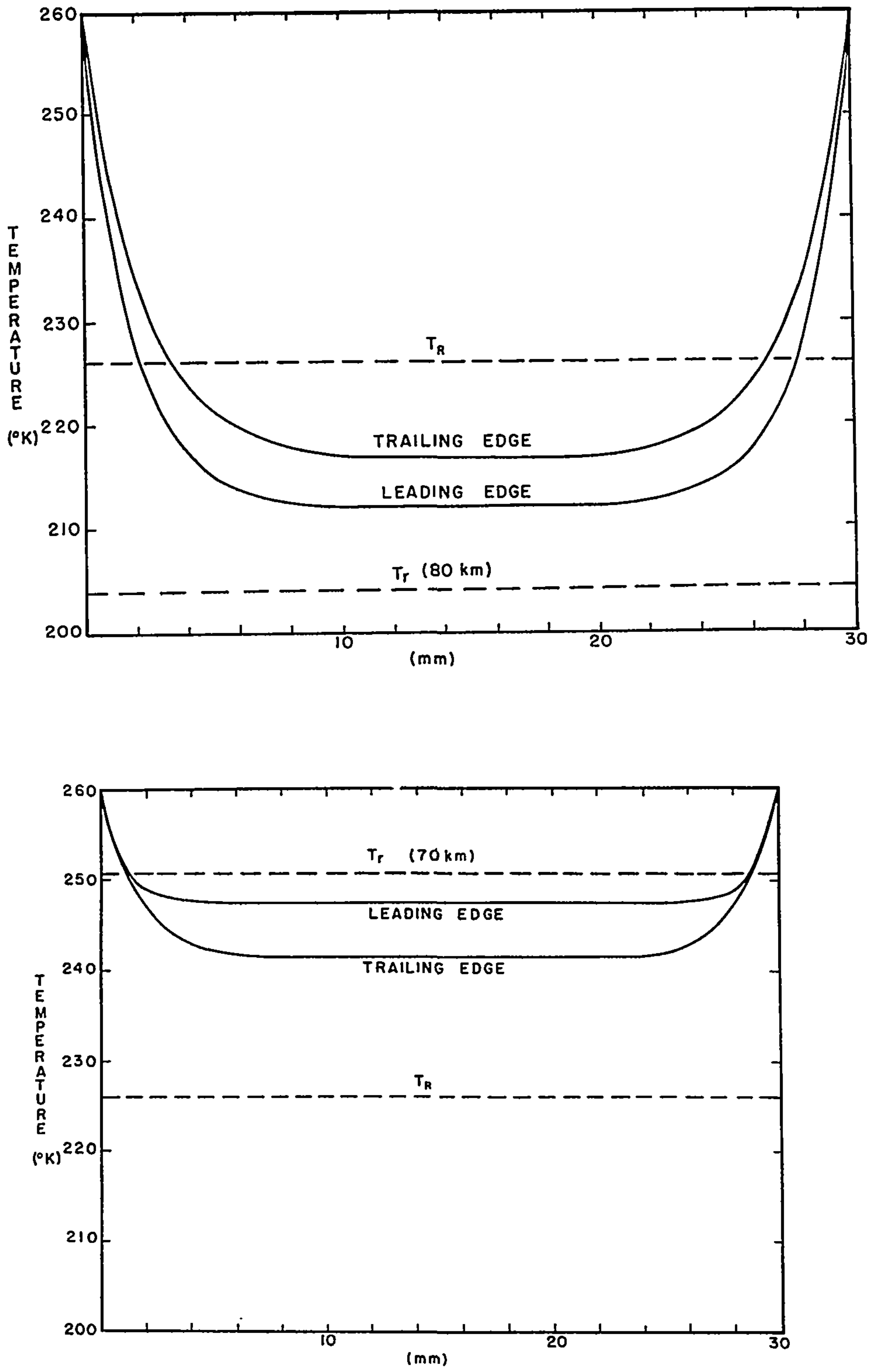

Fig. B3. Temperature distribution over a thin flat plate.

The values of h used in this report for the plate have assumed the temperature detector to be located at the leading edge of the plate, and are therefore based on a characteristic length which is about 3 decay lengths in the plate. Thus h is the mean value of h_x only over a length of the plate downstream which conductively influences the temperature at the leading edge.

A decay length is defined as the length

$$\lambda_f^{-1} = \sqrt{\frac{k\delta}{2\left(h + 4\epsilon\sigma T_a^3\right)}}$$

where λ is the convective parameter in the heat equation

$$\nabla^2 T_f = \lambda_f^2 \left(T_f - T_{fe}\right).$$

Similarly the recovery factor r varies along the flow over the plate. Its local value is taken as that interpolated between the continuum and free molecule values according to

$$r_x = r_c + \frac{K_n\left(r_{fm} - r_c\right)}{K_n + 0.3}$$

where Knudsen number K_n is referred to the boundary layer thickness.

$$K_n = \frac{\lambda}{\delta} = \frac{\lambda}{x}\frac{\sqrt{Re_x}}{7.2}\;, \quad Re_x = \frac{\rho V x}{\mu}$$

Note that since $r_{fm} > r_c$, both K_n and r_x increase toward the leading edge. Aerodynamic heating therefore is greater at the leading edge.

Again, the effective value of recovery factor for the plate in the vicinity of the leading edge is taken as the mean value

$$\overline{r}(L) = \frac{1}{L} \int_0^L r_x(x)\, dx$$

where L is the characteristic length chosen equal to three decay lengths, or the physical length of the plate, whichever is smaller. Figure B4 illustrates $r_x(x)$ and $\overline{r}(x)$ at selected air speeds and altitudes.

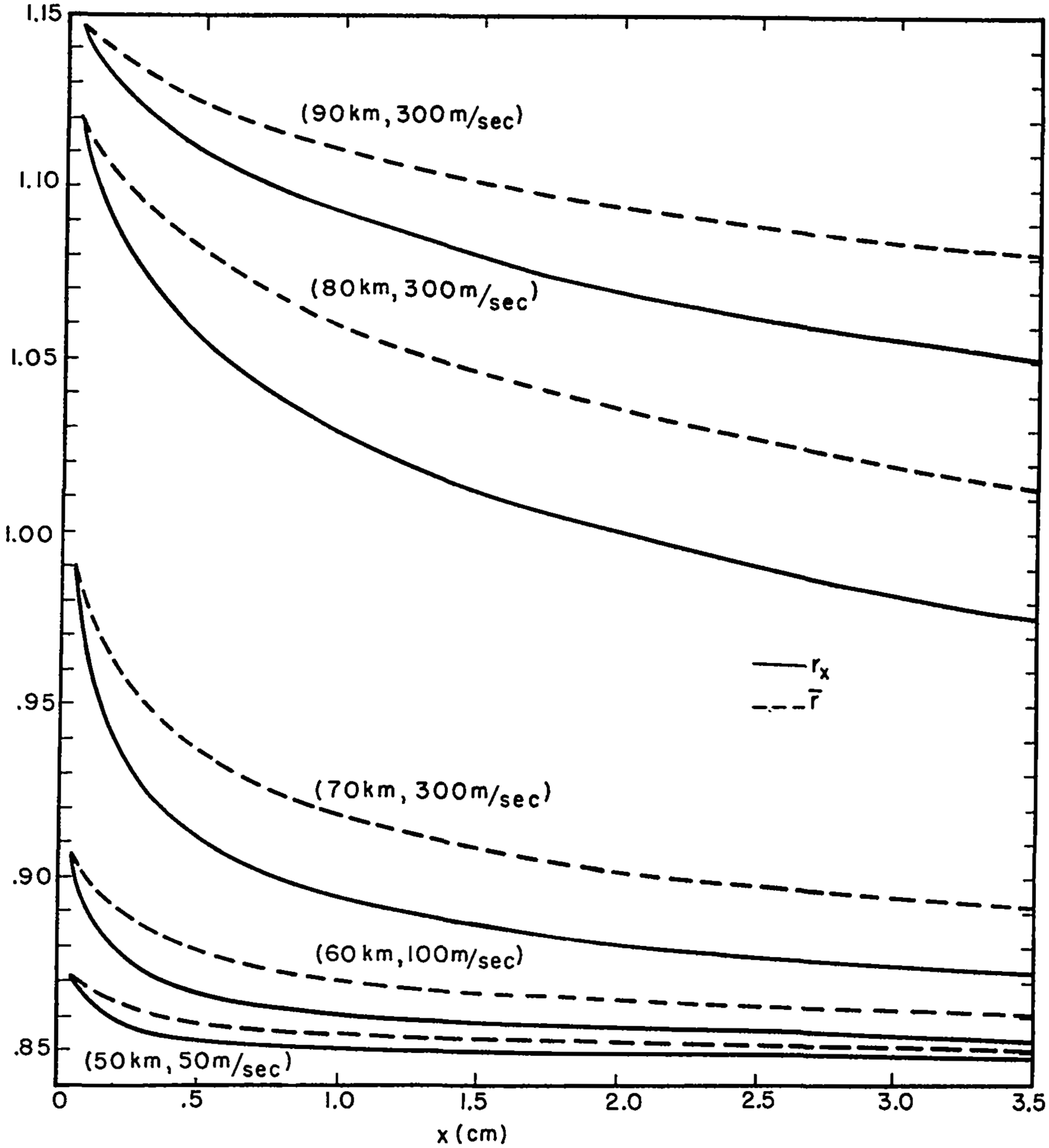

Fig. B4. Local and mean recovery factor for 50 m/sec at 50 km, 100 m/sec at 60 km and 300 m/sec at 70, 80, and 90 km.

NUMERICAL VALUES USED IN COMPARATIVE COMPUTATIONS

c_p = 1004 $m^2/°K\ sec^2$

D = 3.2×10^{-4} m

d = 2.5×10^{-5} m

I_j = $.64558 \times 10^8$, 460.7, 233.8, 3.64 $watt/m^2$

k_w, k_c, k_f = 31, 5, 3.8 watt/m °K

ℓ = 3.2×10^{-3} m

r_o = 10^{-3} m

W = 10^{-5} watt

x = 10^{-3} m

α = ϵ = 0.08

α_s = 0.15

δ = 1.27×10^{-5} m

θ_o = 35°

$(\rho c)_b$, $(\rho c)_{w,c}$, $(\rho c)_f$ = 3.31, 2.71, 1.8 $megajoule/m^3$

σ = 5.67×10^{-8} $watt/m^2\ °K^4$

GLOSSARY

A	total sensor surface
A_o	cross-sectional area of conductive path at the edge of the thermistor region
c	specific heat of sphere, cylinder, or plate
c_p	specific heat of air
C_{wb}	conductive coupling coefficient between wire and bead
C_{wf}	conductive coupling coefficient between wire and film
D	diameter of sphere
d	diameter of cylinder
$E_{b\lambda}(T)$	Planck radiant energy spectral distribution function for a radiation source at temperature T
f_j	geometric factor for jth source
H	$h + 4\epsilon\sigma T_a^3$
H_k	conduction coefficient
h	convective heat transfer coefficient
I_j	radiant emittance of jth source
k	thermal conductivity of the sensor
ℓ	length of wire in bead-wire-film sensor
q_r	radiation heat input
r	recovery factor
r_o	radius of thermistor region on film sensor
S	dissipation constant
T	temperature of the sensor

T_a	nominal temperature of sphere, cylinder, or plate for linearization of T^4
T_e	equilibrium temperature ($\dot{T} = 0$)
T_k	conduction temperature
T_R	radiation temperature
$\dot{T}$	time rate of change of sensor temperature
T_r	recovery temperature
T(env)	atmospheric temperature
u	$h/4\epsilon\sigma T_a^3$
v	volume of sensor
V	air speed
W	electric power dissipation
x	length of thermistor region on filament
α	long-wave absorptivity
α_s	solar absorptivity
α_λ	spectral absorptivity of the sensor
$\bar{\alpha}_j$	mean absorptivity relative to the jth source
β_j	radiation input perturbation factor
δ	thickness of plate
ϵ	emissivity
ϵ_λ	spectral emissivity
Ω	solid angle subtended by the environment at the sensor
θ	angle between sensor surface element dA and the direction toward $d\Omega$
λ	radiation wavelength

λ_f, λ_w, λ_c	inverse of the decay length in an extended convecting body
σ	Boltzmann constant
ψ	aspect angle to the sun
ρ	mass density of the sensor
τ	time constant

<u>Subscript</u>

$j = 1$	sun
$j = 2$	earth as a reflector of solar radiation
$j = 3$	earth and atmosphere as a long-wave source
$j = 4$	sonde parts in view of the sensor as a long-wave source
b	sphere
w	cylinder
c	filament type sensor
f	plate
p	film type sensor

REFERENCES

1. Coulson, K. L., "Effect of Surface Properties on Planetary Albedo," paper presented at American Institute of Aeronautics and Astronautics Thermophysics Specialist Conference, Monterey, California, September 1965.

2. Eddy, A., C. E. Duchon, F. M. Haase, and D. R. Haragan, "Determination of Winds from Meteorological Rocketsondes," Atmospheric Science Group, College of Engineering, The University of Texas, Report No. 2, Contract No. DA-23-072-AMC-1564, November 1965.

3. Haas, G., and L. Hadley, American Institute of Physics Handbook, D. F. Gray, Editor, 2nd Edition, Mcgraw-Hill Book Company, New York, 1963, pp. 6-103.

4. Handbook of Chemistry and Physics, 42nd Edition, Chemical Rubber Publishing Company, Cleveland, Ohio, 1966.

5. Handbook of Chemistry and Physics, 47th Edition, Chemical Rubber Publishing Company, Cleveland, Ohio, 1966.

6. Niederer, Peter G., "Development of a High Altitude Stokes Flow Decelerator," Astro Research Corporation report ARC-R-236, prepared under Contract No. NAS5-10168 for NASA Goddard Space Flight Center, 4 November 1966.

7. Powell, R. W., C. Y. Ho, and P. E. Liley, "Thermal Conductivity of Selected Materials," National Standard Reference Data Series, National Bureau of Standards-8, NSRDS-NBS-8, November 25, 1966.

8. Staffanson, Forrest L. "Mathematical Model of the Film-Mounted Rocketsonde Thermistor," University of Utah paper presented at the American Meteorological Society Conference on High Altitude Meteorology and Space Weather, Houston, Texas, March 31, 1967.

9. Thompson, Donald C., "The Accuracy of Miniature Bead Thermistors in the Measurement of Upper Air Temperatures," AFCRL-66-773, Scientific Report No. 1, Contract No. AF 19(628)-4165, Project No. 6670, Task No. 667001, October 1966.

10. Wagner, N. K., "Theoretical Time Constant and Radiation of a Rocketsonde Thermistor," Journal of Meteorology, Vol. 18, 1961.

NASA-Langley, 1969 — 13 CR-1286